Nonrigid Coregistration of Diffusion Tensor Images Using a Viscous Fluid Model and Mutual Information

Wim Van Hecke*, Alexander Leemans, Emiliano D'Agostino, Steve De Backer, Evert Vandervliet, Paul M. Parizel, and Jan Sijbers

***Abstract*—In this paper, a nonrigid coregistration algorithm based on a viscous fluid model is proposed that has been optimized for diffusion tensor images (DTI), in which image correspondence is measured by the mutual information criterion. Several coregistration strategies are introduced and evaluated both on simulated data and on brain intersubject DTI data. Two tensor reorientation methods have been incorporated and quantitatively evaluated. Simulation as well as experimental results show that the proposed viscous fluid model can provide a high coregistration accuracy, although the tensor reorientation was observed to be highly sensitive to the local deformation field. Nevertheless, this coregistration method has demonstrated to significantly improve spatial alignment compared to affine image matching.**

***Index Terms*—Coregistration, diffusion tensor imaging, mutual information, tensor reorientation, viscous fluid model.**

I. Introduction

DIFFUSION tensor magnetic resonance imaging (DT-MRI, or DTI) provides a unique way to investigate the microstructure of biological tissue [1]. Because it can be assumed that the orientation and magnitude of the local diffusion process, and thus the resulting local diffusion tensor (DT) field, is related to the orientation of the underlying fiber network, DTI can provide an insight into the complex white matter (WM) architecture [2]. The potential impact of DTI is very high in a wide range of WM disorders, since it is the main technique that can model and examine the diffusion process, and thus the brain connectivity, in an *in vivo* and noninvasive way [3]–[8]. DTI has indeed been applied successfully in various neurological and psychiatric studies, demonstrating WM alterations across populations [9], [10].

Voxel-based morphometry (VBM) is a whole brain technique that allows the detection of regionally specific differences in brain tissue composition on a voxel-by-voxel basis. An important requisite for these VBM studies is the development of a high-dimensional, nonrigid coregistration technique, which is able to align both the spatial and the orientation information of multisubject DT images.

The objective of coregistration is to search for the spatial transformations that map different images to a common reference space, in which direct comparison of various image properties is possible [11], [12]. In neuroscience research, it is common practice to coregister images from different individuals into this reference space. In this way, the variability across subjects can be studied or quantitative image properties can be compared between normal volunteers and patients. Especially VBM studies, in which the objective is to quantify various properties of corresponding voxels across different subjects, require an accurate coregistration method for obtaining a robust and reliable outcome of the statistical analysis.

It is generally assumed that global affine transformations—consisting of translations, rotations, shearing, and scaling—are inadequate for intersubject coregistration, since local morphological differences between different subjects can not be taken into account [13]. The transformations needed for intersubject coregistration require to accommodate both complex and large deformations. Nonrigid coregistration techniques utilize such local deformation fields for the image alignment, and are thus, in theory, more adequate to correct for these intersubject variations.

The coregistration of DT images is particularly challenging compared to aligning scalar images, since each DTI voxel is represented by a symmetric second rank tensor, i.e., the six components describing the three-dimensional diffusion process. Consequently, scalar coregistration algorithms have to be adapted so that they can deal with these multicomponent data sets. In addition, the alignment of the DT field with the underlying microstructure has to be preserved after the coregistration process. For the latter, a tensor reorientation (TR) strategy has to be performed [14]. Since Alexander *et al.* raised the TR problem, their proposed TR strategies have been applied widely [14], [15]. The finite strain (FS) method decomposes the transformation matrix in a deformation and a rotation component, whereafter only the latter is used to reorient the tensors. However, shearing, nonuniform scaling and stretching factors affect the orientation as well. Together with the rotational component, they are taken into account in the preservation of principal direction (PPD) strategy. In this study, the PPD algorithm is implemented as described by the direct DT reconstruction approach of Leemans *et al.* [16].

The most trivial approach to coregister DTI data is by registering scalar images associated with the DTI data sets, such as

Manuscript received June 1, 2007; revised July 22, 2007. This work by supported by the Institute for the Promotion of Innovation through Science and Technology in Flanders (IWT-Vlaanderen). *Asterisk indicates corresponding author*.

*W. Van Hecke is with the VisionLab, Department of Physics, University of Antwerp, 2610 Antwerp, Belgium.

A. Leemans is with the CUBRIC, Cardiff University, CF10 3AT Cardiff, U.K.

E. D'Agostino is with the Medical Image Computing, University of Leuven, B-3000 Leuven Belgium.

S. De Backer and J. Sijbers are with the VisionLab, is with the VisionLab, Department of Physics, University of Antwerp, 2610 Antwerp, Belgium.

E. Vandervliet and P.M. Parizel are with the Department of Radiology, University Hospital Antwerp, 2650 Edegem, Belgium and also with the Faculty of Medicine, University of Antwerp, B-2610 Antwerp, Belgium.

Color versions of one or more of the figures in this paper are available online at http://ieeexplore.ieee.org.

Digital Object Identifier 10.1109/TMI.2007.906786

0278-0062/$25.00 © 2007 IEEE

T_2-weighted MR images, fractional anisotropy (FA) maps, or the nondiffusion weighted (DW) images [17], [18]. Alexander and Gee proposed a multiresolution elastic matching algorithm and introduced similarity measures based on the DT data [19]. Ruiz–Alzola *et al.* optimized affine transformations in certain restricted windows of the image domain, measuring image correspondence based on DT data [20], [21]. Note that in [19] and [21], no TR was applied during the optimization.

Park *et al.* and Guimond *et al.* extended the demons algorithm to DTI data and applied an iterative TR strategy [22]–[24]. This iterative tensor adaptation increases the algorithmic complexity and computation time drastically. Furthermore, although the DT information is more exploited compared to [19] and [21], errors caused by an imperfect TR can affect the alignment at each iteration. In addition, no initial correction is performed for the presence of voxel intensity differences in corresponding structures of different data sets or subjects, caused by a different brain morphology. This potentially results in a nonoptimal starting point of the sum of squared distances (SSD) similarity measurement. Finally, Zhang *et al.* proposed a local affine coregistration algorithm using DT data in the similarity measure in order to optimize the tensor reorientation explicitly [25].

In this paper, a nonrigid coregistration algorithm based on a viscous fluid model is proposed that has been optimized for DTI images. D'Agostino *et al.* already demonstrated the potential of this model for the coregistration of scalar MR images [26]. Since, in contrast to the elastic model, the viscous fluid approach is not limited to small displacements and small rotation angles of the deformation field, it is very suitable for intersubject coregistration tasks [27]. Multiple DTI information components, such as the DT elements or the DW images, are integrated into the coregistration technique. In an attempt to tackle the aforementioned iterative TR issues, we propose mutual information *(MI)* as a criterion for DT image similarity [28]–[30]. *MI* has been shown to work in many applications, even when the relationship between the image intensities is complicated or unknown [30]. In the proposed coregistration technique, no TR is performed in an iterative way, assuming that *MI* is a robust measure of the image similarity, even when the tensors are not reoriented during registration. This reduces the computational complexity drastically. Therefore, in this work, the tensors are only reoriented after the application of the final deformation field. In order to evaluate the ability of *MI* to compare the nonreoriented tensor data during the iterative alignment procedure, our results are compared with an analogous method in which the TR is applied iteratively. Our coregistration results demonstrate that the spatial and orientation alignment is significantly improved compared to an affine image matching. In addition, the tensor reorientation was observed to be highly sensitive to the local deformation field.

II. Multicomponent Viscous Fluid Coregistration

A. Viscous Fluid Model

The general goal of coregistration is to map a particular floating image $\phi(\vec{x})$ to a reference image $\tau(\vec{x})$ in order to align both. In the following framework, the images are modelled as a viscous fluid. Such a viscous fluid model, which imposes constraints on the local deformation field during coregistration, can be described by the free-form nonrigid coregistration algorithm of [31], in which a regularization function from elasticity theory has been applied [26], [31]. D'Agostino *et al.* replaced this elastic model with a viscous fluid regularization model of Christensen *et al.*, which allows the viscous fluid model to be described by the following simplified Navier–Stokes equation [26], [27], [32]:

$$\mu\nabla^2\vec{v} + (\mu+\lambda)\vec{\nabla}(\vec{\nabla}\cdot\vec{v}) + \vec{F}(\vec{x},\vec{u}) = \vec{0} \tag{1}$$

with $\vec{v}$ the deformation velocity and $\vec{F}$ the force field, which depends on the local deformation $\vec{u}$ and the deformation position $\vec{x}$. The material parameters μ and λ are set to 1 and 0, respectively [27]. At each iteration k of the gradient descent optimizer of the coregistration algorithm, the new displacement $\vec{u}^{(k+1)}$ is calculated from the previous displacement $\vec{u}^{(k)}$, taking into account the perturbation $\vec{R}^{(k)}$ of the deformation field and the time step parameter $\Delta t^{(k)}$

$$\vec{u}^{(k+1)} = \vec{u}^{(k)} + \vec{R}^{(k)}\Delta t^{(k)}. \tag{2}$$

In (2), $\vec{R}^{(k)}$ is defined as

$$\vec{R}^{(k)} = \vec{v}^{(k)} - \sum_{i=1}^{3} v_i^{(k)} \left(\frac{\delta\vec{u}^{(k)}}{\delta x_i}\right) \tag{3}$$

with $\vec{v}^{(k)}$ defined as the convolution of the force field $\vec{F}^{(k)}$ and a Gaussian spatial smoothing kernel Ψ_s with a width s [24], [26]

$$\vec{v}^{(k)} = \Psi_s \otimes \vec{F}^{(k)}. \tag{4}$$

The force field $\vec{F}$ is defined in such a way that the viscous fluid deformation strives at maximizing the *MI* between the deformed floating image $\phi(\vec{x}-\vec{u})$ and the target image $\tau(\vec{x})$. To this end, the gradient of the *MI* with respect to an infinitesimally changed deformation field $\vec{u}$ is required [31]. The joint intensity distribution $p_{\vec{u}}^{\phi,\tau}(i_1,i_2)$ of the deformed floating image and the target image is therefore modeled as a continuous function using Parzen windowing, making it differentiable with respect to the deformation field. Hereby, i_1 and i_2 represent the intensities of images ϕ and τ. The *MI* between $\phi(\vec{x}-\vec{u})$ and $\tau(\vec{x})$ can be defined as [30]

$$MI(\vec{u}) = \sum_{i_1}\sum_{i_2} p_{\vec{u}}^{\phi,\tau}(i_1,i_2)\log\frac{p_{\vec{u}}^{\phi,\tau}(i_1,i_2)}{p^{\tau}(i_2)p_{\vec{u}}^{\phi}(i_1)}. \tag{5}$$

Hereby, p^{τ} and p^{ϕ} represent the marginal intensity distributions of τ and ϕ, respectively. The gradient of the *MI* with respect to a deformation field $\vec{u}$ that is perturbed into $\vec{u}+\epsilon\vec{h}$ can be calculated and simplified to [31]

$$\left.\frac{\partial MI(\vec{u}+\epsilon\vec{h})}{\partial\epsilon}\right|_{\epsilon=0} = \sum_{i_1}\sum_{i_2}\left(\left(1+\log\frac{p_{\vec{u}+\epsilon\vec{h}}^{\phi,\tau}(i_1,i_2)}{p^{\tau}(i_2)p_{\vec{u}+\epsilon\vec{h}}^{\phi}(i_1)}\right)\cdot\left.\frac{\partial p_{\vec{u}+\epsilon\vec{h}}^{\phi,\tau}(i_1,i_2)}{\partial\epsilon}\right|_{\epsilon=0}\right). \tag{6}$$

Thereby, the joint intensity distribution $p_{\vec{u}}^{\phi,\tau}(i_1,i_2)$ of the reference and deformed floating image is estimated from the region of overlap v' (with volume V) using a Parzen window kernel $\psi_h(i_1,i_2)$ with width h

$$p_{\vec{u}}^{\phi,\tau}(i_1,i_2)=\frac{1}{V}\int_{v'}\psi_h(i_1-\phi(\vec{x}-\vec{u}),i_2-\tau(\vec{x}))d\vec{x}. \quad (7)$$

The force field can now be written as [26], [31]

$$\begin{aligned}\vec{F}(\vec{x},\vec{u})&=\vec{\nabla}_{\vec{u}}MI\\&=\frac{1}{V}\left[\frac{\delta\psi_h}{\delta i_1}\otimes L_{\vec{u}}\right](\phi(\vec{x}-\vec{u}),\tau(\vec{x}))\,\vec{\nabla}\phi(\vec{x}-\vec{u})\end{aligned} \quad (8)$$

with

$$L_{\vec{u}}(i_1,i_2)=1+\log\frac{p_{\vec{u}}^{\phi,\tau}(i_1,i_2)}{p^{\tau}(i_2)p_{\vec{u}}^{\phi}(i_1)}. \quad (9)$$

The force field, driving the deformation to maximize *MI*, is defined as the gradient of *MI* with respect to $\vec{u}(\vec{x})$, and can be calculated using the intensity gradient of the deformed floating image $\phi(\vec{x}-\vec{u})$, weighted by the impact on the *MI* of a voxel in ϕ at $\vec{x}-\vec{u}$ being displaced in this direction [26], [31]. This force field is calculated at each iteration of the gradient-descent optimization procedure, until the *MI* no longer increases or the Jacobian determinant of the total deformation becomes negative. In this way, it is ensured that the transformation is homeomorphic. At each time step during the deformation, the force field is constant such that the modified Navier–Stokes equation can be solved iteratively as a temporal concatenation of linear equations [26]. A velocity field is obtained by solving the modified Navier–Stokes (1). This velocity field is computed with (4), as in Thirion *et al.* approximating the approach of Bro-Nielsen and Gramkow [24], [33]. Thereafter, the perturbation to the deformation field is computed (3) and used to obtain the displacement field at a given iteration (2).

At each iteration, the determinant of the Jacobian is constrained to reduce the chance that the underlying anatomical microstructure is forced in a physical or anatomical nonacceptable way [34]. When the determinant of the local Jacobian becomes smaller than 0.5, a regridding of the deformed floating image is applied to generate a new floating image, setting the incremental displacement field to zero [32]. A width of $h=4$ and $s=3$ were used for the Gaussian Parzen windowing kernel ψ_h and for the spatial smoothing kernel Ψ_s, as described in [26]. The time step parameter Δt in (2) is adapted each iteration and set to

$$\Delta t^{(k)}=\max(||\vec{R}^k||)\Delta u \quad (10)$$

with Δu (in voxels) the maximal allowed voxel displacement in each iteration. D'Agostino *et al.* demonstrated that an optimal balance between speed of convergence and need for regridding is obtained for $\Delta u=0.6$.

B. Multicomponent Coregistration

In its simplest form, coregistration of DTI data sets is based on the alignment of two scalar T_2-weighted images. Thereafter, the resulting transformation is applied to the DT images. Although T_2-weighted images have a higher spatial resolution compared to DTI, the coregistration result will be strongly affected by the severe lack of white matter contrast in these images. Indeed, conventional MR protocols, such as T_1- or T_2-weighted pulse sequences, represent the white matter as a rather homogeneous region. Since nonrigid coregistration algorithms are mainly driven by the contrast of different brain structures, low contrast regions, such as the white matter on conventional MR images, will be poorly aligned. As a result, the structural and particularly the orientation correspondence will be very low in the white matter after coregistration [23].

In order to provide more structural information to guide the coregistration in white matter regions, DTI features are used. For this purpose, the scalar FA map, containing a high white matter contrast, has demonstrated to be an appropriate feature [17]. In this context, Guimond *et al.* introduced a multicomponent normalization method based on the DT eigenvalue images (λ_1, λ_2, λ_3) [22]. As argued by Alexander *et al.* to preserve the intrinsic information of the tensor, only rigid transformations should reorient the tensors, independent of the nature of the local transformation that is applied [14]. The scalar measures, such as the FA and the eigenvalues, are invariant to rigid transformations, and, therefore, TR is not required during coregistration. Park *et al.* demonstrated that the use of DT elements improved the coregistration quality significantly [23]. They implemented the demons algorithm and used the SSD as a similarity criterion [24].

When the DTI alignment is based on images that contain orientation information, such as the DT components or the DW images, the coregistration problem becomes more complex. In contrast to the voxel intensities of the images that are invariant to rigid transformations, the voxel intensities of the DT components or the DW images are dependent on the position of the subject in the scanner and on the local morphology of the brain. For example, when a particular white matter tract follows a different path in two subjects, its DT or DW intensity values can vary significantly in corresponding voxels, whereas the FA can be similar. Since the intensity variation in corresponding voxels has a local, spatial-dependent nature, image intensity transformations, which are often used to deal with multimodal images, are not applicable under these circumstances. DTI coregistration, that incorporates orientation information to align the images, is, therefore, one of the few applications that has to accommodate both the alignment of intersubject images and the presence of nonlinear intervoxel intensity differences.

In a study of Park *et al.*, a TR was applied iteratively during coregistration using the FS approach [23]. By iteratively adjusting the tensor orientation, the accuracy of the image alignment may be increased. However, the necessity for an iterative tensor adaptation increases the algorithmic complexity and computation time drastically. Furthermore, errors caused by an imperfect TR can affect the alignment at each iteration. Note that, by implementing an iterative TR, no initial correction is performed for the presence of voxel intensity differences in corresponding structures, potentially resulting in a nonoptimal starting point of the SSD similarity measurement. Moreover, FA or eigenvalue image data are known to be non-Gaussian distributed, due to the nonlinearity in the calculation of the

eigenvalue system [35]. Since, the widely used SSD similarity measure presupposes similar voxel intensity values in various images that only differ from each other by a Gaussian noise term, it can, therefore, not be used optimally for this purpose.

In an attempt to mitigate the aforementioned DTI coregistration issues, we propose to use *MI* as a criterion for DT image similarity. By applying *MI*, the nonlinear intervoxel intensity differences are taken into account without the need for an explicit tensor reorientation during the optimization procedure. Consequently, the tensors are only reoriented after the application of the final deformation field. In this study, three different coregistration approaches are evaluated using a different number of components (L): FA map ($L = 1$), the DT elements ($L = 6$), and the DW images ($L = 60$).

C. Mutual Information and Force Field Calculation for Multiple Components

Generally, in the context of coregistration, *MI* is defined and studied between two scalar images, measuring their statistical dependency. The concept of multivariate *MI* was introduced as an extension of the bivariate case to multiple scalar images, thereby constructing a multidimensional histogram [36]. Since the six DT element images or the 60 DW images form multicomponent data, the alignment of two DTI data sets becomes a multivariate coregistration problem. In contrast to the general multivariate problem, the data sets in the multicomponent DTI coregistration process can be subdivided in two groups ϕ_l and τ_k that represent multicomponent (DT or DWI) images of two different data sets ($l = 1, \ldots, L$ and $k = 1, \ldots, K$). Applying the general multivariate idea of evaluating statistical dependencies for each image combination to this specific problem, would increase the computation time dramatically. Therefore, some adjustments are introduced to adapt the general multivariate space to the specific multicomponent DTI problem.

First, only images that have the same number of components are coregistered ($L = K$). Indeed, DT elements of data set ϕ_l are compared with DT elements of data set $\tau_k (L = K = 6)$, and the DW images of ϕ_l are compared with the DW images of $\tau_k (L = K = 60)$. Second, only cross-subject statistical dependencies are computed. The different components of data set ϕ_l are not compared with each other (and analogous for data set τ_k), thereby assuming that all image components of a single subject are aligned. Third, the corresponding components are evaluated in parallel ($l = k$). For example, the first DT element image of data set ϕ_l (i.e., ϕ_1) is compared with the first DT element image of data set τ_k (i.e., τ_1), and never with another DT element image of data set τ_k. In this way, the general multivariate space is simplified with respect to the specific multicomponent coregistration problem of DT images. Rohde *et al.* proposed a multivariate correlation approach for the coregistration of multicomponent images [37]. However, by using correlation coefficients, the assumption is made that a linear relationship is present between the intensity values of the different components of different subjects.

We propose two similarity metrics based on the statistical dependencies of the multicomponent DT images. Both represent a summary metric on the original multivariate space, based on *MI*.

"*MI* method 1"

In a first approach for the calculation of the multicomponent *MI*, the bivariate *MI* is computed for all L corresponding components separately, assuming them to be independent. A similar approach was adopted in Park *et al.* using the sum of squared distances as a similarity metric [23]. A global measurement of image similarity is proposed by averaging the MI_l of the different corresponding components: $MI = (1/L)\sum_{l=1}^{L} MI_l$. This *MI* metric is optimized in the iterative coregistration process. At each iteration, the force field of (8) is calculated for all corresponding components separately

$$\vec{F}_l(\vec{x}, \vec{u}) = \frac{1}{V_l}\left[\frac{\delta\psi_h}{\delta i_1} \otimes L_{l,\vec{u}}\right](\phi_l(\vec{x} - \vec{u}), \tau_l(\vec{x})) \cdot \vec{\nabla}\phi_l(\vec{x} - \vec{u}) \tag{11}$$

with $L_{l,\vec{u}}$ based on the joint intensity histogram of corresponding image component l. In this way, L force fields are calculated independently, based on the gradient of its corresponding floating image component and weighted by the effect on the *MI* between the corresponding floating and reference image component. A final force field is calculated as an average force field of all corresponding components $\vec{F} = (1/L)\sum_{l=1}^{L} \vec{F}_l$. This force field $\vec{F}$ is then used to calculate the velocity field (4), whereafter the perturbation to the deformation field (3) and the displacement field (2) are computed at each iteration. This deformation field is applied to all L components of the floating image, ϕ_l, which is then used as the floating image in the next iteration.

"*MI* method 2"

In a second approach, the global *MI* is calculated from a histogram that already contains all information of the different components simultaneously. All components of a data set are concatenated to a single image. Thereafter, the global joint intensity histogram can be calculated on both concatenated images $\vec{\phi}$ and $\vec{\tau}$, containing all information of the L components. The *MI* is based on this global joint intensity histogram and can now be written as

$$MI(\vec{\phi}, \vec{\tau}) = \sum_{i_1}\sum_{i_2}\left(p^{\vec{\phi}\vec{\tau}}(i_1, i_2) \cdot \log\left(\frac{p^{\vec{\phi}\vec{\tau}}(i_1, i_2)}{p^{\vec{\phi}}(i_1)p^{\vec{\tau}}(i_2)}\right)\right) \tag{12}$$

with i_1 and i_2 representing the voxel intensities and

$$\vec{\tau} \equiv [\tau_1, \ldots, \tau_L] \quad \vec{\phi} \equiv [\phi_1, \ldots, \phi_L] \tag{13}$$

denoting the collection of selected components of the floating image and the reference image, respectively. In practice, the multicomponent image information is pooled into a single histogram, by adding the joint histograms of all image components. This histogram is then less sparse and contains all information of the histograms of the corresponding components. The *MI* of (12), containing information of all image components, is optimized during the iterative coregistration process. In (12), $p^{\vec{\phi},\vec{\tau}}$ is the joint intensity distribution of the images $\vec{\phi}$ and $\vec{\tau}$, and $p^{\vec{\phi}}$ and $p^{\vec{\tau}}$ represent the marginal intensity distributions of $\vec{\phi}$

and $\vec{\tau}$, respectively. In this approach, they are calculated as a sum of the histograms of the corresponding components

$$p^{\vec{\phi}\vec{\tau}}(r,f) = \frac{1}{L}\sum_{i=1}^{L} p^{\phi_i\tau_i}(r,f)$$
$$p^{\vec{\tau}}(r) = \frac{1}{L}\sum_{i=1}^{L} p^{\tau_i}(r)$$
$$p^{\vec{\phi}}(f) = \frac{1}{L}\sum_{i=1}^{L} p^{\phi_i}(f). \quad (14)$$

Analogous as in "*MI* method 1," the force field of (8) is calculated for all corresponding segments

$$\vec{F}_l(\vec{x},\vec{u}) = \frac{1}{V}\left[\frac{\delta\psi_h}{\delta i_1}\otimes L_{\vec{u}}\right](\phi_l(\vec{x}-\vec{u}),\tau_l(\vec{x}))\cdot\vec{\nabla}\phi_l(\vec{x}-\vec{u}). \quad (15)$$

In contrast with "*MI* method 1," the $L_{\vec{u}}$ is based on the total joint intensity histogram of images $\vec{\phi}$ and $\vec{\tau}$. Again, L force fields are calculated based on the image gradient of each component. However, the force field weighting factors are now driven by the global *MI* of (12). The global force field is computed as an average of all L component force fields: $\vec{F} = (1/L)\sum_{l=1}^{L}\vec{F}_l$. This force field is then used to calculate the velocity field (4), whereafter the new deformation field $\vec{u}$ can be derived with (2) and (3). Finally, all floating image components are iteratively updated by the application of the deformation field.

III. Acquisition and Evaluation Methodology

In this section, the DTI acquisition parameters and the evaluation setup are first described (Sections III-A and III-B). Then, the measures that are used to evaluate the coregistration method are presented in Section III-C. Finally, the statistical tests are introduced for the interpretation of the results (Section III-D).

A. Acquisition

DTI measurements of the human brain were performed with a 1.5 T MR scanner on 40 healthy subjects (16 males and 24 females), with a mean age of 28 years (19–55 years). An informed consent was signed by all participants. Axial DT images were obtained using a SE-EPI sequence with the following acquisition parameters: TR $= 10.4$ s; TE $= 100$ ms; diffusion gradient $= 40\,\mathrm{mT\cdot m^{-1}}$; FOV $= 256\times256\,\mathrm{mm^2}$; number of slices $= 60$; image resolution $= 2\times2\times2\,\mathrm{mm^3}$; $b = 700\,\mathrm{s\cdot mm^{-2}}$; acquisition time $= 12$ min 18 s. Diffusion measurements were performed along 60 directions for a robust estimation of FA, tensor orientation, and MD [38]. All DTI post processing, such as calculation of the eigenvalue system and the visualization, was performed with the diffusion toolbox "ExploreDTI"[1] [39].

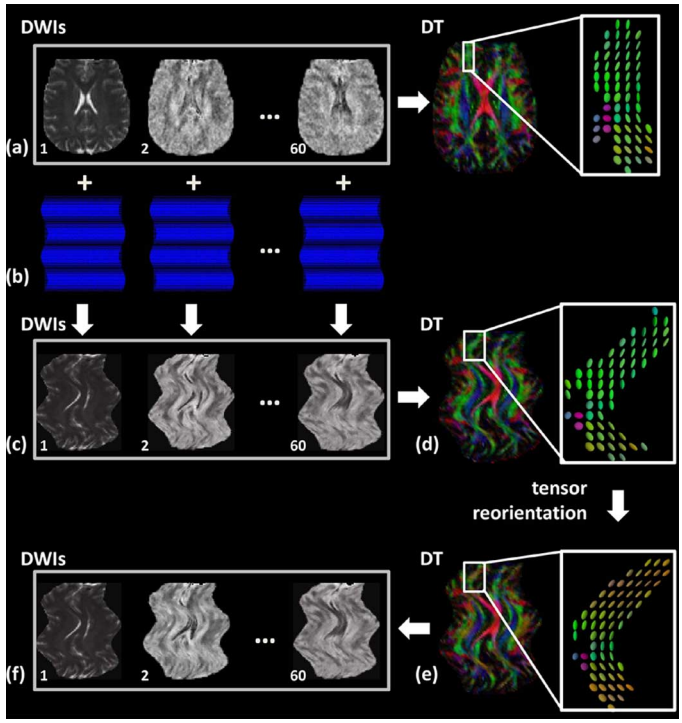

Fig. 1. DW images of a DTI data set (a) are deformed with a known deformation field (b), resulting in a set of deformed DW images (c). DT elements are calculated from these deformed DW images (d). Thereafter, a tensor reorientation is performed to realign the deformed tensors with their underlying microstructure (e). Finally, the DW images are recalculated from the realigned DT elements (f) to construct the deformed DT data set that is used as a floating image in the coregistration algorithm. The DT maps are color encoded according to the diffusion direction.

B. General Setup

All images are first coregistered to a randomly chosen single subject image with an affine coregistration algorithm that is designed for DTI, thereby using the MIRIT (multimodality image registration using information theory) method [16], [30]. In order to evaluate our proposed viscous fluid coregistration method, two approaches are followed.

- The first evaluation approach, using 15 different nonrigid, predefined deformation fields, can be summarized as follows (see Fig. 1).
  - — A predefined deformation field is applied to the DW images of an original DTI data set. This original DTI data set is referred to as the reference image [see Fig. 1(a) and (b)].
  - — The DT field is calculated from the deformed DW images [see Fig. 1(c) and (d)].
  - — The DT are reoriented to preserve the alignment with the underlying, deformed microstructure [Fig. 1(e)].
  - — The DW images are recalculated from the reoriented DT field, resulting in the deformed data set, also referred to as the deformed data or floating image [Fig. 1(f)].

[1]http://www.dti.ua.ac.be

— The deformed data set [Fig. 1(f)] is coregistered spatially to the reference data set [Fig. 1(a)], followed by a TR of the DT field and a recalculation of the DW images. Since the difference between the deformed and the reference image is predefined, it can be regarded as ground-truth to evaluate the subsequent coregistration.

- To examine the applicability of our coregistration technique for VBM studies or the formation of a connectivity atlas, DT images of 40 different persons are normalized, and an arbitrary chosen data set is used as a reference image.

Multiple DTI components and *MI* calculation methods are used in both coregistration evaluation approaches, and are numbered as follows.

I Affine coregistration.

Viscous fluid coregistration using the

II FA maps;
III DT elements and "*MI* method 1;"
IV DT elements and "*MI* method 2;"
V DWI elements and "*MI* method 1;"
VI DWI elements and "*MI* method 2."

C. Evaluation Measures

Only voxels with an FA value larger than 0.4 are considered in the quantitative analysis. Although these selected voxels do not strictly form a WM segmentation, they are referred to as the WM mask in the remainder of this paper. Both the spatial coregistration result and the orientation correspondence are evaluated as follows.

- When the theoretical deformation field is known, a quantitative value can be assigned, comparing the final transformation after coregistration with the ground-truth deformation for each voxel B

$$C_B = \frac{||\vec{s}_B - \vec{s'}_B||}{||\vec{s}_B|| + ||\vec{s'}_B||}. \tag{16}$$

  Here, $\vec{s}_B$ and $\vec{s'}_B$ represent the theoretical and final deformation field, respectively. The median of C_B of all selected voxels, referred to as C, can then be interpreted as an overall measure of the transformation field correspondence. When C is 0, the final deformation field exactly equals the theoretical deformation field, representing a perfect spatial alignment. On the other hand, when C is 1, the final deformation field is the opposite of the theoretical deformation field, resulting in the worst alignment.
- In order to evaluate the coregistration technique with respect to the orientation information, the angle a_B between the first eigenvector of the reference image $\vec{n}_B$ and the transformed floating image $\vec{n'}_B$ can be calculated for each WM voxel B

$$a_B = \cos^{-1}\left(\frac{\left|\vec{n'}_B \cdot \vec{n}_B^T\right|}{||\vec{n'}_B|| \cdot ||\vec{n}_B||}\right). \tag{17}$$

  The median a of all selected voxels B is a measurement of the preservation of orientation information after coregistration, since it represents a general value of the first eigenvector alignment. The smaller this first eigenvector angle difference, the better the orientation alignment between the images involved. Another measure which we will apply in our evaluation method is the overlap of eigenvalue-eigenvector pairs between tensors [40]

$$OVL = \frac{1}{N_B}\sum_B \frac{\sum_{i=1}^{3} \lambda_i \lambda'_i \left(\vec{\epsilon'}_i \cdot \vec{\epsilon}_i^T\right)^2}{\sum_{i=1}^{3} \lambda'_i \lambda_i} \tag{18}$$

  with N_B the total number of selected WM voxels, and λ'_i, λ_i, and $\vec{\epsilon'}_i, \vec{\epsilon}_i$ eigenvalues and eigenvectors of the deformed floating image and the reference image, respectively. The minimum value 0 indicates no overlap and the maximum value 1 represents complete overlap of the principal axes of the DT field.

D. Statistics

The nonparametric Wilcoxon matched-pairs signed-rank test is applied to find the potential statistical significant difference between the coregistration results. On the other hand, a paired t-test is used to interpret the intersubject alignment results.

IV. Results

In Section IV-A, the orientation of the DT field after deformation of the DTI data set is evaluated on synthetic DTI phantoms [41]. Next, Section IV-B presents the viscous fluid coregistration results with respect to accuracy and as a function of the amount of image noise. Additionally, a qualitative example is provided. In order to investigate the effect of nonrigid deformation fields on the subsequent TR, different TR methodologies, applied after the viscous fluid coregistration, are evaluated (Section IV-C). In Section IV-D, the methodology without an iterative TR is compared with a method that performs an iterative TR. Finally, the effect of different thresholds for defining the white matter masks for quantitative evaluation will be examined in Section IV-E.

A. TR Evaluation Using Synthetic DTI Data Sets

In this section, the TR approaches are evaluated for the nonrigid coregistration using a synthetic DTI phantom [41]. An estimation of the error caused by the TR itself is important for the interpretation of the tensor correspondence after coregistration.

The synthetic DTI data experiments for the evaluation of the TR techniques can be summarized as follows.

- The DW images of a straight, synthetic fiber bundle d_1 were deformed with different nonrigid, sinusoidally shaped deformation fields, resulting in a deformed bundle d_2 [analogous as in Fig. 1(a)–(c)].
- The DT field was calculated from the deformed DW images of d_2 [analogous as in Fig. 1(d)].

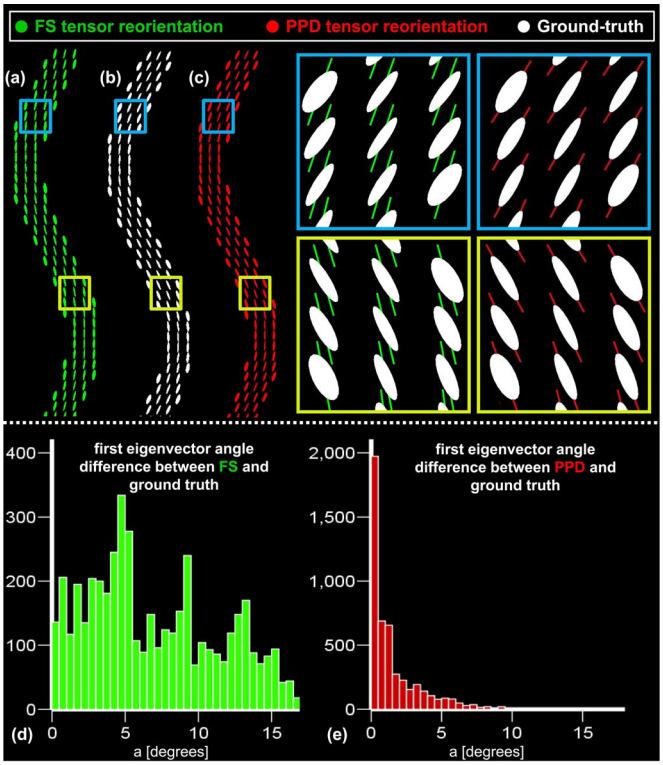

Fig. 2. First, a straight, synthetic fiber bundle is deformed with a nonrigid, sinusoidally shaped deformation field. A TR is subsequently performed, using the FS (a) and the PPD (c) approach. Second, a sinusoidally shaped, synthetic fiber bundle with exactly the same frequency and amplitude as the aforementioned deformation field is defined (b). The orientation of these diffusion tensors can be regarded as ground-truth. The white ellipsoids represent the ground-truth tensors and the first eigenvectors after FS and PPD tensor reorientation are superimposed in green and red, respectively. The first eigenvector angle difference between the ground-truth and the TR result is displayed in (d) for the FS TR, and in (e) for the PPD TR.

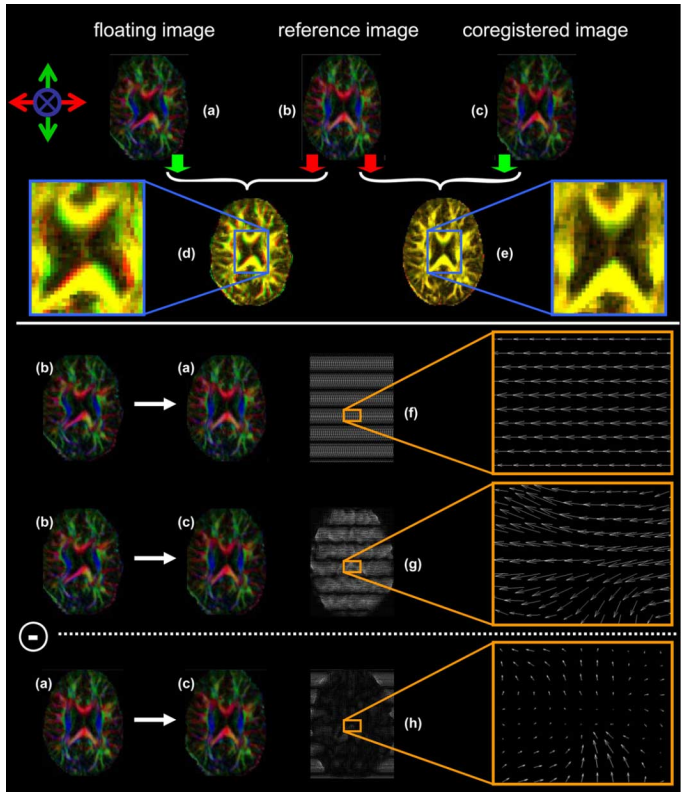

Fig. 3. Qualitative coregistration result of a synthetic DTI data set. The reference DT image, given in (b), is deformed with a predefined deformation field [see (f)], resulting in the image as displayed in (a). For the following coregistration analysis, this deformed data set is used as the floating image, whereas the data set in (b) is used as the reference image. The coregistered image is shown in (c). In order to evaluate the image correspondence visually, the FA intensity map of the reference image is given a red color, whereas the FA intensities of the floating and coregistered images are given a green color. Consequently, when the reference and floating image are overlapping, a yellow color is indicated (d). Therefore, this can be used to visually detect the correspondence quality of the coregistration. An analogous image is composed for the reference and the coregistered images (e), demonstrating a better image alignment after coregistration. In order to get a more detailed view of the alignment, the different vector fields are displayed in (f)–(h). In (f), the predefined, ground-truth deformation field used to deform the reference image (b) to the floating image (a) is shown. The final deformation field after coregistration of the floating image (a) to the reference image is displayed in (g). After subtraction of these vector fields, the spatial coregistration error can be visualized in (h).

- In order to realign the DT field with the deformed microstructure, a TR was performed with the FS and the PPD method [see Fig. 2(a) and (c), respectively].
- The DW images were recalculated from the reoriented DT field [analogous as in Fig. 1(f)].
- In order to evaluate the TR approaches, a ground-truth is necessary. Therefore, a new synthetic fiber bundle d_3 was simulated [see Fig. 2(b)]. This bundle exhibits a sine function trajectory with exactly the same frequency and amplitude as the aforementioned deformation fields that were used to deform the first straight bundle. The DT field of d_3 was regarded as ground-truth, since it exactly follows the spatial pattern of the defined white matter fiber bundle.
- The DT field of d_2 after TR was then compared with the ground-truth DT field of d_3, as displayed in Fig. 2.

In order to quantify the tensor difference, the angle between the first eigenvectors of the deformed and the ground-truth tensors was calculated in each selected WM voxel. For the FS tensor reorientation method, the median angle was $7^\circ \pm 4^\circ$. Since the PPD TR technique clearly outperforms the FS method, with a median angle of $1.6^\circ \pm 1.5^\circ$, it was implemented to reorient the tensors *a priori* with a predefined deformation field resulting in the ground truth data sets.

These deformed data sets are used in Section V as the floating images that are coregistered to the reference DTI data set. In order to align the DT field with the underlying microstructure after coregistration to the reference image, both FS and PPD strategies were applied. In this way, the effect of local coregistration inaccuracies on the TR result is studied.

B. Multicomponent Viscous Fluid Coregistration

1) Qualitative Coregistration Results: An example of the alignment of a DTI data set, deformed with a predefined deformation field, to the reference image is shown in Fig. 3. In Fig. 3(a)–(c), the deformed data set, the ground-truth DT image, and the coregistered image are displayed, respectively. In order to evaluate the image correspondence before coregistration, the FA map of the reference image is given a red color, and the FA map of the (deformed) floating image is given a green color. Therefore, when both images are overlayed [see Fig. 3(d)],

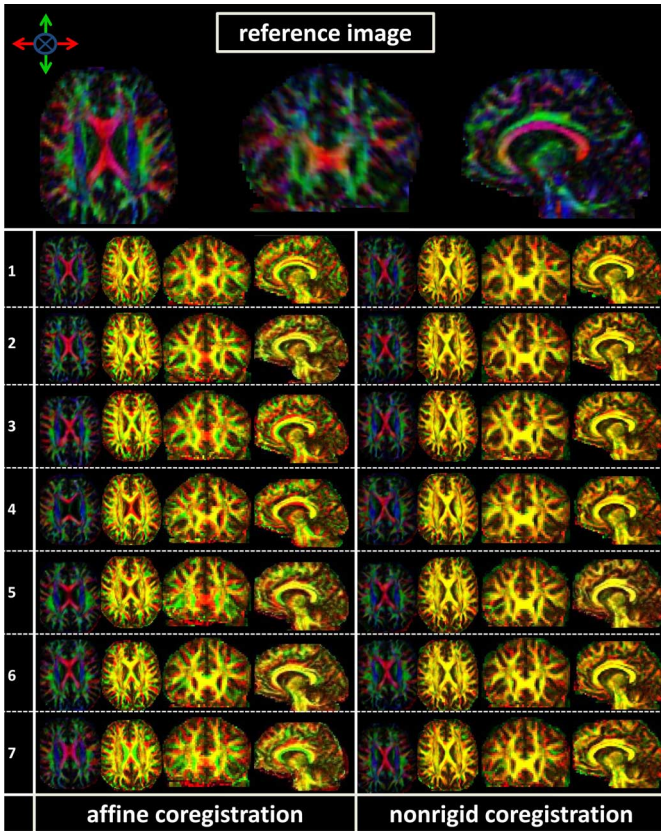

Fig. 4. At the top of this figure, an axial, coronal, and sagittal slice of the reference data set are shown. The color is encoded according to the diffusion direction. In the bottom part of this figure, seven arbitrarily chosen images of different subjects are shown after affine (left column) and a subsequent viscous fluid model based (right column) coregistration with the reference image. In each column, the diffusion direction encoded axial slices of the coregistered data set are shown on the left. The other images are composed of the red colored FA intensity values of the reference image on the one hand, and the green colored FA intensity values of the coregistered image on the other hand. The yellow color indicates that similar FA intensities are present in corresponding voxels.

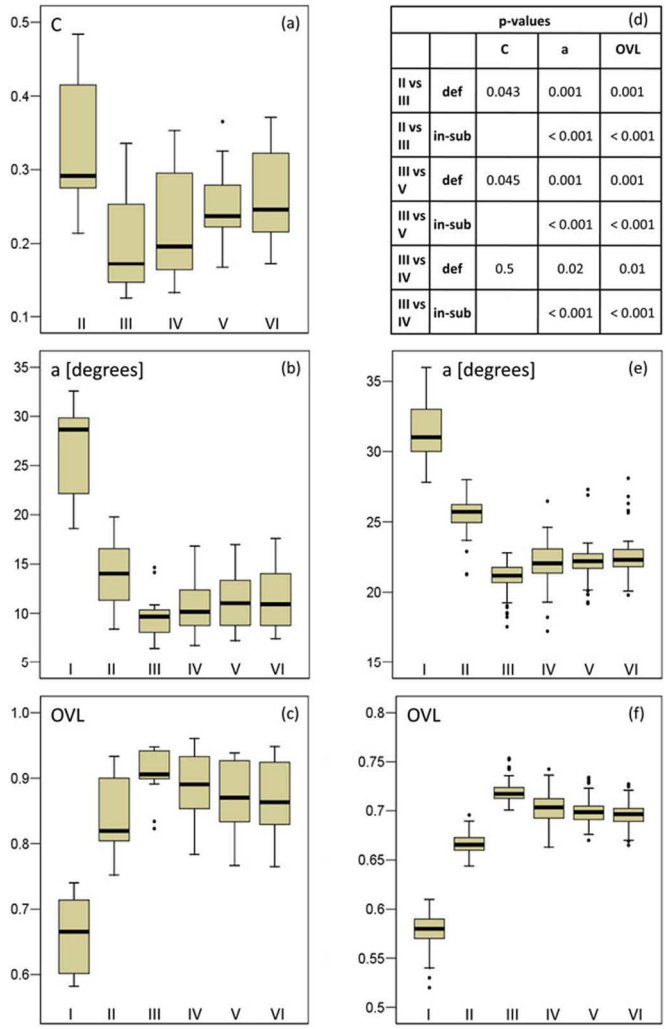

p-values		C	a	OVL
II vs III	def	0.043	0.001	0.001
II vs III	in-sub		< 0.001	< 0.001
III vs V	def	0.045	0.001	0.001
III vs V	in-sub		< 0.001	< 0.001
III vs IV	def	0.5	0.02	0.01
III vs IV	in-sub		< 0.001	< 0.001

(d)

Fig. 5. Quantitative coregistration results of deformed data sets with known deformation fields and intersubject data are shown on the left and right, respectively. The different coregistration methods are grouped on the horizontal axis. (I) represents the affine result, (II) is the FA based coregistration, (III) uses DT components and iteratively averages the mutual information during coregistration, and (IV) uses DT components and calculates the global histogram from all DT elements. Method (V) and (VI) are analogous to (III) and (IV), respectively, but use the DW images as information components. Parameter C calculates the correspondence of the final deformation field after coregistration with the predefined deformation field (a). The angle difference a between the first eigenvectors of corresponding voxels of different data-sets is displayed in the middle row for the deformed (b), and intersubject (e) DTI data. In (c), and (f) the OVL, measuring the eigenvalue-eigenvector overlap of tensors in corresponding voxels, is given for the deformed, and intersubject data, respectively. Finally, in (d), the p-values between the coregistration methods are shown for the quantitative parameters.

corresponding voxels that contain similar intensity values in the reference and floating image will appear yellow after overlaying both images. Similar maps are shown after viscous fluid coregistration [see Fig. 3(e)]. The theoretical deformation field [between Fig. 3(a) and (b)] and the obtained deformation field after coregistration [between Fig. 3(a) and (c)] are displayed in Fig. 3(f) and (g), respectively. The difference between these deformation fields is presented in Fig. 3(h), demonstrating a high vector field correspondence and a subvoxel mean vector field error.

An axial, coronal, and sagittal representation of the intersubject coregistration result is given in Fig. 4. Again, the FA map of the reference image was given a red color, whereas the FA map of the affine and nonrigid coregistration result were both given a green color. Consequently, the overlay of the reference image (red) with the affine and nonrigid coregistration maps (green) will display a yellow color when correspondence is high, and a red or green color when the correspondence is low.

2) Evaluation Measures of the Coregistration: Quantitative coregistration results of DTI data sets deformed with predefined deformations are shown in Fig. 5(a)–(c). The FS approach was applied to reorient the DT field after coregistration. In Fig. 5(e) and (f), the first eigenvector angle difference a and OVL are displayed for intersubject data. The quantitative results, displayed in Fig. 5, demonstrate that the nonrigid coregistration method clearly outperforms the affine alignment results. In addition, the use of multiple components (methods III-VI) always resulted in an improved alignment, compared to the FA coregistration. This amelioration is furthermore statistically significant in the case of deformed data with a predefined deformation field and in the case for intersubject data (see Fig. 5(d): II versus III). In Fig. 5(d) (III versus V), it is demonstrated that the coregistration based on the DT elements outperformed the DWI coregistration outcome. It is

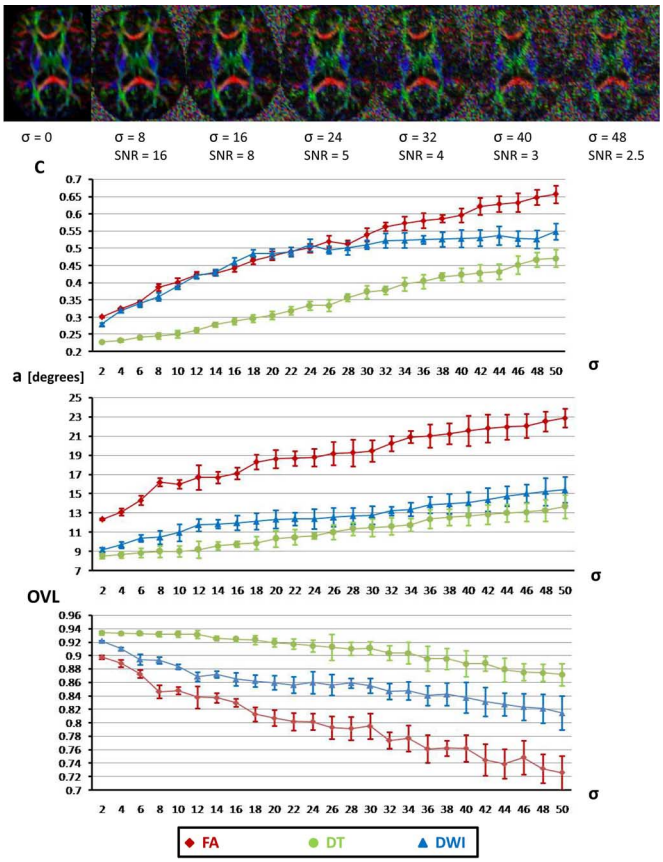

Fig. 6. Different levels of Rician noise, represented by σ are added to the DW images. A visual presentation of the noise DTI data is given at the top. The color is hereby encoded according to the predominant diffusion direction. At the bottom of the figure, the spatial and orientation correspondence are given using the FA map (method (II) of Fig. 5), the DT elements (method (III) of Fig. 5), and the DW images (method (V) of Fig. 5) as coregistration components. C, a, and OVL represent the deformation field correspondence, the first eigenvector angle difference, and the eigenvalue-eigenvector overlap, respectively.

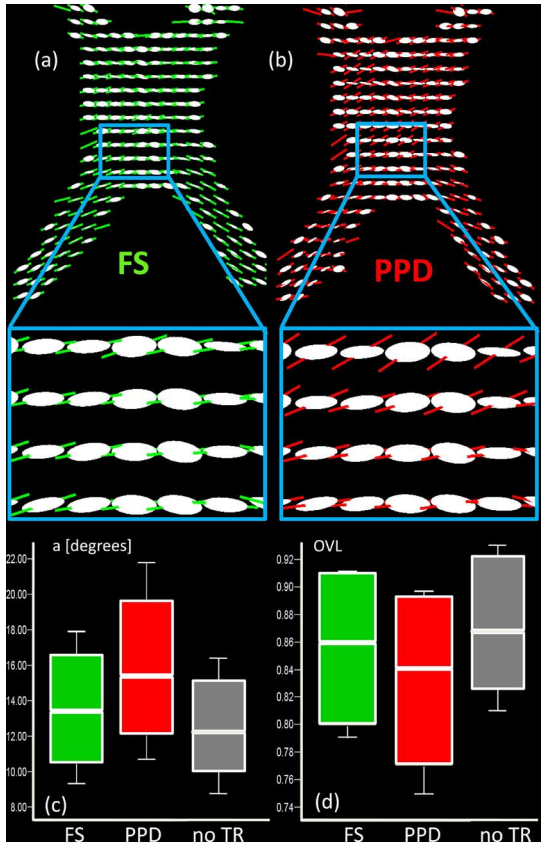

Fig. 7. In (a) and (b), a part of the corpus callosum as seen on an axial slice is shown. The white ellipsoids represent the ground-truth tensors of the reference image. The FS (in green) and PPD (in red) TR result after nonrigid coregistration are superimposed by means of the first eigenvector in (a) and (b), respectively. The first eigenvector correspondence with the ground-truth a and OVL of the the tensor reorientation approaches are presented in (c), and (d), respectively. These results originate from the coregistration of deformed data with a predefined deformation field, based on the FA maps, but are similar when other components are used. Note the higher tensor correspondence, when no tensor reorientation (in grey) is performed [(c) and (d)].

furthermore shown that the calculation of the global *MI* on one histogram, containing all components, does not result in a better alignment, compared to the iterative averaging of all component *MI*s. Especially in the case of intersubject data, the latter difference is statistically significant, whereas this is not always the case for the deformed data (see Fig. 5(d): II versus IV).

3) Effect of Noise: In order to study the effect of noise on the coregistration outcome, the reference and the DW images, deformed with a known deformation field, were corrupted with different levels of Rician distributed noise (represented by σ). Next, all DTI features were calculated from the noisy DW images. After coregistration, a transformation is found for each voxel from the floating image to the reference image. Instead of applying this deformation field to the noisy floating image, it is used to transform the floating image without noise. In this way, quantitative values described in Section III-C, give insight into the effect of noise on the alignment error itself.

In Fig. 6(a)–(c), the alignment results are displayed in the presence of different levels of noise. Notice that, even when very high noise levels are added, the image alignment, and especially the orientation correspondence, is still preserved. The upper part of Fig. 6 displays an axial DTI slice, corrupted with different levels of noise. The SNR measure is defined as the average intensity value of all diffusion weighted images divided by the level σ of the Rician distributed noise that is added.

C. Tensor Reorientation After Nonrigid Coregistration

1) Comparison of FS and PPD Tensor Reorientation Methods: In paragraph Section IV-A, we demonstrated that the PPD method outperformed the FS approach when applied after the deformation with a smooth, known deformation field. In contrast to what was expected, the FS technique outperformed the PPD approach when applied after coregistration, as can be seen in Fig. 7. Furthermore, this difference is statistically significant $(p < 0.001)$. These results are obtained from the FA image coregistration of 10 data sets that were first deformed with a predefined deformation field. Equivalently, these findings were analogous to the other methods, in which other components were used for the coregistration. In Fig. 7(a) and (b), a part of the corpus callosum is displayed on an axial slice. Here, the white ellipsoids represent the ground-truth tensors of the reference image. The first eigenvector, as obtained after FS and PPD reorientation are superimposed in Fig. 7(a) and (b), respectively. In Fig. 7(c) and (d), the first eigenvector angle difference a and OVL are compared between both TR techniques.

Another remarkable result was observed when no TR was performed after coregistration. This method outperformed the FS and PPD tensor reorientation methodologies with respect to the tensor alignment, as described by a and OVL [see Fig. 7(c) and (d)]. For the intersubject coregistration, the following results were derived for the FS approach, PPD method, and without TR, respectively (for a random group of 15 persons, using the FA maps): $a = 26.3^\circ \pm 1.2^\circ$, $29.4^\circ \pm 1.3^\circ$, and $23.6^\circ \pm 1.2^\circ$; $OVL = 0.66 \pm 0.01$, 0.63 ± 0.02, and 0.68 ± 0.01. Similar results were found when other DTI information components were used for the coregistration.

2) Effect of the Coregistration Inaccuracies on the Tensor Reorientation: Although, in theory, the PPD method outperforms the FS approach (see paragraph Section IV-A), results turn out to be worse than the results of the FS approach when applied after the nonrigid viscous fluid deformation field (see Fig. 7). In addition, tensors are better aligned when no TR is applied. These unexpected results can be explained by the fact that, because there are less constraints on the local level of coregistration, small coregistration inaccuracies, which hardly affect the spatial alignment result, can occur, having a severe impact on the subsequent tensor reorientation. We hypothesize that these alignment errors contain more skewness and scaling than rotational components, thereby having a larger effect on the PPD than on the FS TR approach. The latter is verified by decomposing the Jacobian of the coregistration inaccuracies into a rotation component on the one hand, and a deformation component—containing scaling- and skewness factors—on the other hand.

The error Jacobian is constructed from the vector field difference between the theoretical and the obtained deformation field after coregistration. The rotation and the deformation component are calculated from the error Jacobian as follows:

$$R_e = \left(U_e U_e^T\right)^{-1/2} U_e \quad S_e = U_e R_e^{-1} \tag{19}$$

with R_e the rotation and S_e the deformation component, and $U_e = I + J_e$, where I is the identity matrix and J_e is the Jacobian, calculated on the error field [14], [42]. Note that U_e, R_e, and S_e are 3×3 matrices that are attributed to each voxel, describing the local transformation, rotation, and deformation, respectively. In order to study the presence of rotation and deformation components in the error Jacobian, the magnitude of U_e, R_e, and S_e is calculated. This is done by taking the following Frobenius matrix norms $N_J \equiv ||U_e - I||^2$, $N_R \equiv ||R_e - I||^2$, and $N_S \equiv ||S_e - I||^2$ for each WM voxel.

For the deformed data with known deformation fields, the aforementioned matrix norms averaged over all voxels within the WM mask, are $N_J = 0.55 \pm 0.05$, $N_R = 0.22 \pm 0.03$, and $N_S = 0.42 \pm 0.05$, for the transformation, rotation, and deformation, respectively. These results indicate that the contribution of rotations is much smaller compared to the contribution of the skewness and scaling factors in the Jacobian of the alignment inaccuracies. Furthermore, they confirm the hypothesis that the PPD is more affected by local, small coregistration errors compared to the FS approach, resulting in a worse first eigenvector correspondence.

3) Deformation Field Regularization: In order to improve the TR, an isotropic Gaussian smoothing of the obtained deformation field is performed. This regularization is performed after the coregistration process and is only used to improve the accuracy of the Jacobian matrices of the global deformation. It will, therefore, not affect the spatial alignment of the images. The results after deformation field regularization are presented in Fig. 8 both for the deformed data with a known deformation field, and intersubject data. It is clear that especially the PPD results are improved by this regularization. In Fig. 8(a) and (b), the quantitative results for the regularization procedure of the data deformed with a predefined deformation field are presented for both TR methods and different deformation field smoothing kernel widths, represented by s. In Fig. 8(d) and (e), the final vector field and the error field before smoothing are displayed. The same vector fields are presented in Fig. 8(h) and (i), after a Gaussian smoothing of the final deformation field with a kernel width of three voxels. In Fig. 8(f) and (g), a small part of the corpus callosum, similar to that in Fig. 7, is displayed. Here, the white ellipsoids represent the ground truth of the reference image and the first eigenvectors of the FS and PPD method after coregistration are superimposed in green and red, respectively. The large first eigenvector difference of the PPD approach with the ground-truth in Fig. 8(g) is decreased when the final deformation field is regularized, as can be seen in Fig. 8(k). In contrast to this, the FS result does not show a visual improvement in this restricted part of the corpus callosum after deformation field regularization [see Fig. 8(j)]. A similar analysis is performed with 15 randomly chosen intersubject data [Fig. 8 (l) and (m)]. These quantitative and visual results confirm the hypothesis that especially the skewness, and scaling factors will be regularized, thus particularly improving the PPD results. Above a specific kernel smoothing width, the PPD method outperforms the FS approach. The Frobenius norms of the Jacobian, rotation, and deformation matrices of the error field further validate this hypothesis. As can be seen in Fig. 8(c), N_S is reduced up to the level of N_R during deformation field regularization with different kernel widths.

While initially the results without TR were better compared to the results after TR, the tensor reorientation methods outperform the approach without the TR when a deformation field regularization is applied (see Figs. 7(c) and (d) and 8(a) and (b) for the simulated data results). For the intersubject coregistration without TR, a and OVL were $23.4^\circ \pm 1.1^\circ$ and 0.680 ± 0.014, respectively. Results after final deformation field smoothing are better compared with these results [see Fig. 8 (l) and (m)]. Furthermore, the Wilcoxon matched-pairs signed-rank test demonstrates that the difference between results with TR and without TR are statistically significant for both the simulated and the intersubject data $(p < 0.05)$.

A similar deformation field regularization is performed on data sets containing different levels of Rician noise. It is clear that the FS method outperforms the PPD when no smoothing of the final deformation field is performed [Fig. 9 (a) and (b)]. For an arbitrary noise level of $\sigma = 6$, the effect of the proposed regularization method is shown in Fig. 9(c) and (d). If the kernel width is larger than two voxels, the PPD method outperforms the FS approach. In Fig. 9 (e) and (f), the coregistration results

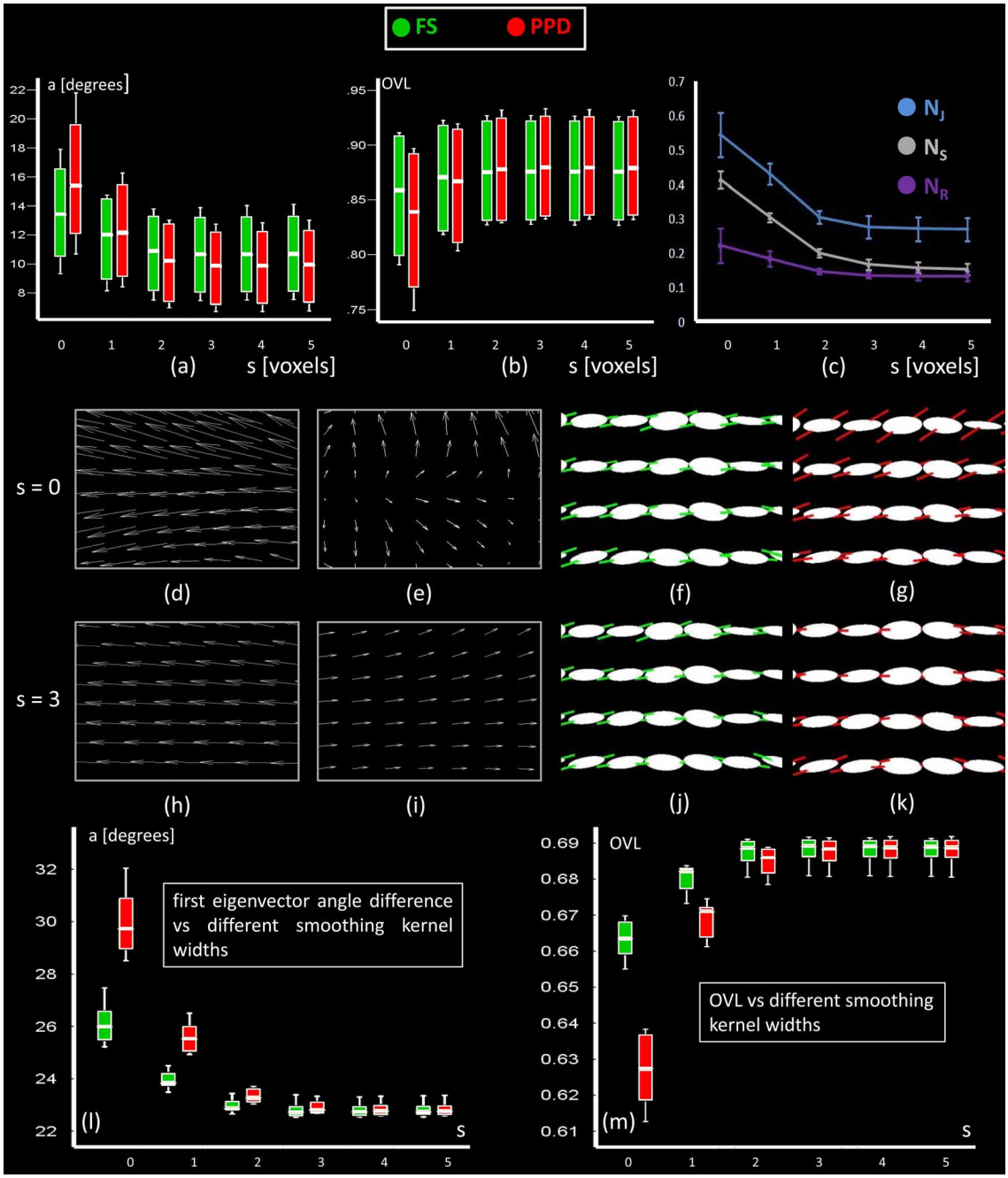

Fig. 8. The first eigenvector angle difference and OVL are given in (a) and (b), respectively, for both the FS and PPD method, using different Gaussian smoothing kernels for the deformation field regularization. In (c), the transformation N_J, rotation N_R, and deformation N_S of the error field are displayed for different smoothing kernel widths. The obtained deformation field before and after smoothing is given in (d) and (h), respectively. The error field before and after filtering is displayed in (e) and (i), respectively. The first eigenvector alignment for a part of the corpus callosum after FS and PPD TR are shown in (f) and (g) before smoothing, and in (j) and (k) after smoothing. The white ellipsoids represent the ground-truth orientations of the reference image. These results are obtained from data deformed with predefined deformation fields. The first eigenvector correspondence a and the tensor overlap with the ground-truth are given in (l) and (m), respectively, for the intersubject results.

as a function of different levels of Rician distributed noise are displayed, in which deformation field smoothing has been performed with a kernel width of three voxels.

D. Iterative Tensor Reorientation

When the DTI alignment is based on images that contain orientation information, like the DT components or the DWIs, voxel intensities of various data sets can have different values in corresponding structures. Therefore, *MI* was used as an image similarity metric to take into account the potential nonlinear intervoxel intensity relationship. In this context, no TR was applied during the iterative optimization process, which results in a reduced computational time. In order to evaluate the ability of *MI* to compare the nonreoriented tensor data, the results are compared with a similar method in which the TR is applied iteratively. In Fig. 10, the first eigenvector angle difference a, the OVL, and the computation time are shown for the method without an iterative TR [Fig. 10(a) and (b)], a

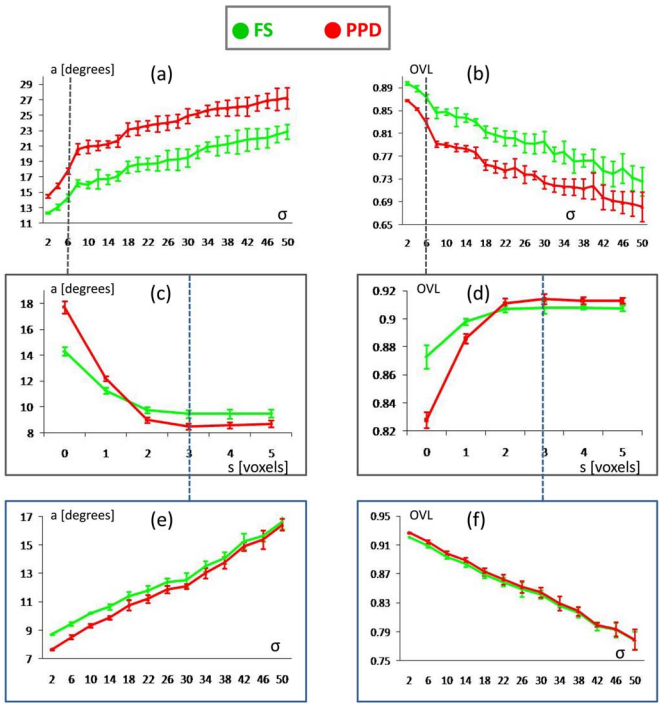

Fig. 9. Different levels of Rician noise, represented by σ are added to the DW images. The orientation correspondence after coregistration is calculated for both TR methods as a function of these different noise levels [(a) and (b)]. At an arbitrary noise level of $\sigma = 6$, the effect of deformation field regularization is shown [(c) and (d)]. In (e) and (f), the same noise study is performed, but now the deformation field, as obtained after coregistration, is smoothed with a kernel width of three voxels.

method with an iterative FS based TR [Fig. 10(c) and (d)], and a method using an iterative PPD based TR [Fig. 10(e) and (f)]. Fig. 10 (a), (c), and (e) represents the coregistration results of 10 deformed images with a predefined deformation field, whereas Fig. 10 (b), (d), and (f) shows the results of the 10 intersubject coregistrations. All results of Fig. 10 are derived after DT based coregistration, in which the *MI* and force field are calculated with "*MI* method 1." Furthermore, for all approaches, the FS method was used for the tensor reorientation on the final deformation field without applying a Gaussian smoothing on the final deformation field.

E. Use of Different WM Masks

All previous results are obtained by only selecting FA mask voxels with an FA value above 0.4. In Fig. 11(a) and (b), the first eigenvector angle difference a, and the OVL, respectively, are displayed as a function of the FA mask threshold. The blue line represents the results without a final deformation field regularization. The results derived after Gaussian smoothing of the final deformation field with a kernel width of three voxels are displayed in purple. In Fig. 11(c), a scatter plot of the FA value and the first eigenvector angle difference is shown. The scatter plot of the FA value and the OVL is displayed in Fig. 11(d). The voxels used for this analysis were obtained from a specific region around the corpus callosum within the coregistered data set. Analogous scatter plots of the same data sets are displayed in Fig. 11(e) and (f), in which a deformation field regularization is applied with a kernel width of three voxels.

V. Discussion

The aim of this paper was to explore the feasibility of a nonrigid viscous fluid model for the alignment of intersubject DTI data sets. First, we investigated the use of multiple DTI information components with respect to the coregistration accuracy. Second, different measures were introduced to calculate the *MI* and the viscous fluid force field. Finally, a thorough investigation of the diffusion tensor reorientation methods was performed.

A. TR Evaluation Using Synthetic DTI Data Sets

The errors that are found between the reoriented and the ground-truth tensors in the synthetic DTI data analysis (see Fig. 2) are not affected by noise factors or coregistration inaccuracies, since the deformation fields are perfectly known and the sinusoidal fiber bundle matches the deformed straight bundle exactly. Alexander *et al.* demonstrated that PPD tensor reorientation after application of a known, affine deformation field to synthetic data, resulted in a mean angle difference of $0° \pm 0°$ when compared with the ground-truth data set [14]. In contrast with these results, we observed a small, but significant tensor difference. Therefore, even if two images are spatially aligned in a theoretically perfect way, tensor orientation errors will occur. These errors originate from the nonrigid nature of the deformation fields and the accompanying interpolation artifacts. Note that the use of Log-Euclidean metrics can further minimize these interpolation errors and potentially improve the image similarity [43].

B. Multicomponent Viscous Fluid Coregistration

Overall, the results of Figs. 3 and 4 indicate the potential of our proposed coregistration technique to coregister intersubject DTI data. In these figures, it can clearly be observed that the alignment errors can be minimized using the viscous fluid coregistration method as compared to the affine DT image alignment. These coregistration results are confirmed by the quantitative analysis, as can be seen in Figs. 5 and 8. Both for the synthetic data and the multisubject brain DTI data sets, the average angle between the first eigenvectors of the coregistered and the reference image is relatively small. In addition, the DT correspondence, as measured with the OVL, is relatively large, compared to the results of Park *et al.* [23]. It should be mentioned, however, since they used a WM mask derived from SPM on MR-images, in contrast to our FA value based WM mask, this comparison should be considered with great caution.

Although all available information is present in the DWIs, the DT elements demonstrated to provide the best result for intersubject coregistration. In our opinion, this can be explained by the reduction in dimensionality through the fitting of a DT to the DW data. The DT data are more compact and still contain the orientational diffusion information. In addition, coregistration using the DT data is less sensitive to noise than using the DW data.

Two image similarity measures, based on *MI*, are proposed that represent a summary metric on the multivariate space. The general multivariate space is simplified to two multicomponent data sets with the same length, whereby only corresponding

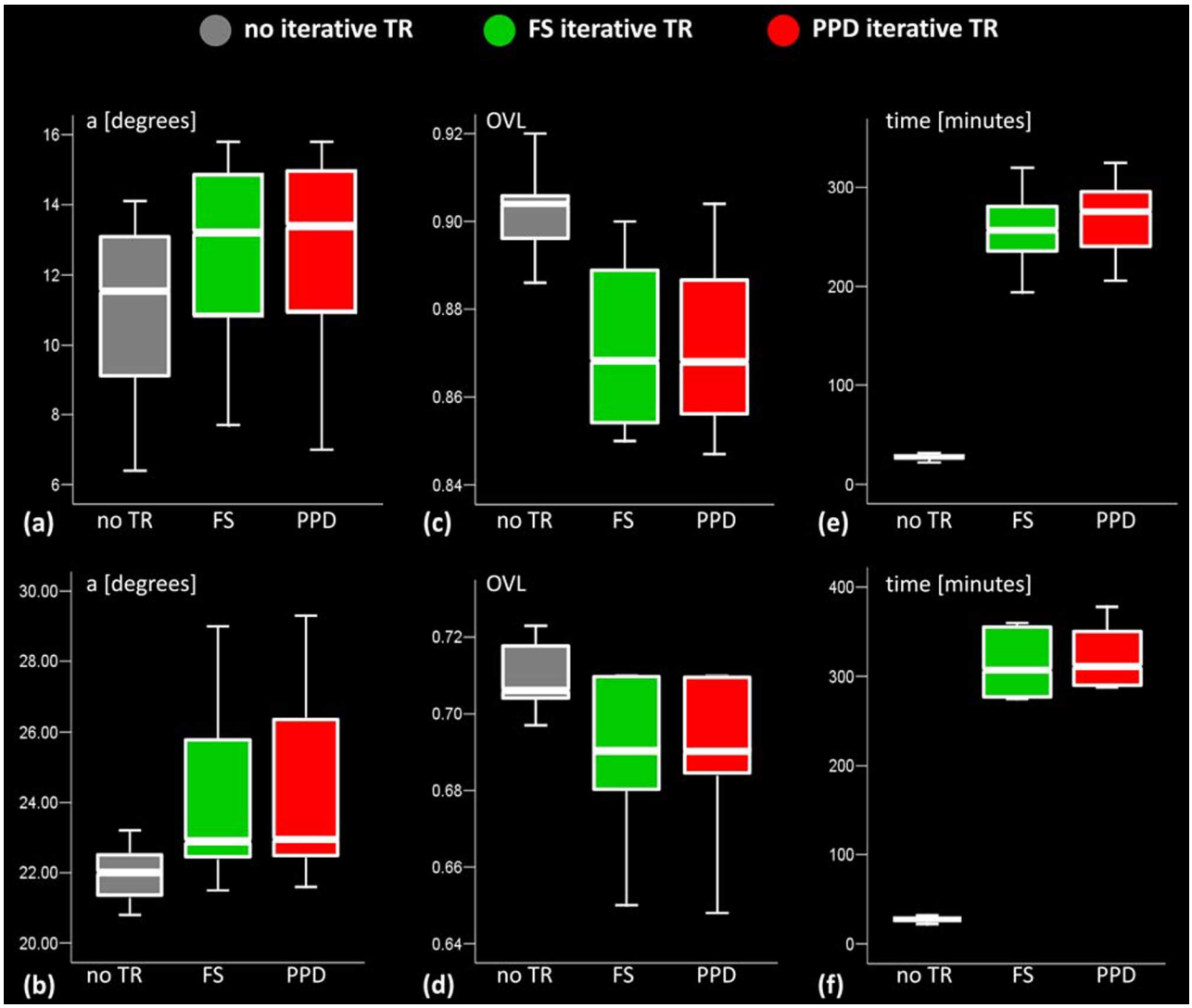

Fig. 10. First eigenvector angle difference a [(a) and (b)], the OVL [(c) and (d)], and the computation time [(e) and (f)] are displayed for different iterative tensor reorientation approaches. Images (a), (c), and (e) result from a coregistration of 10 deformed DTI data sets with a predefined deformation field, whereas images (b), (d), and (f) result from an intersubject coregistration of 10 DTI data sets.

components of different data sets are compared, assuming alignment of the components of each data set *a priori*. The first image similarity metric averages the *MI* of the different components, which is done in a similar way with the SSD measure as described in the work of Park *et al.* [23]. The second image similarity metric pools all data into a single histogram, whereafter the *MI* is calculated on this histogram. This methodology can be seen as the histogram and *MI* computation on two images that are composed of a concatenation of all components in each data set. Since *MI* is a statistical measure, it can be biased by a lack of data in the histogram. This bias of a sparse histogram is minimized by pooling all multicomponent image information into this single histogram. Our results demonstrated that this methodology does not outperform the method of averaging the *MI* of all components. However, when only a small number of data is available for the histogram calculation, as in a window based coregistration of for example Ruiz–Alzola *et al.*, the methodology using the pooled histogram would be favorable [21].

Since both proposed similarity metrics in the simplified multivariate space remain ad-hoc, more research is planned to improve the similarity metric based on *MI* for the multicomponent DTI problem.

When noise was added to the DW images, image alignment worsened. Note that large noise levels were added, resulting in a small SNR. The DT based coregistration outperformed the DWI based alignment after the addition of Rician noise to the DWIs.

C. Tensor Reorientation After Nonrigid Coregistration

Alexander *et al.* studied the behavior of both TR methods under affine and nonrigid conditions [14], [15]. When three different DTI data sets of a same person were aligned affinely, both TR strategies showed almost identical results, since the transformation mainly contained rigid components [14]. The PPD method just outperformed the result without TR and the FS method, when two DTI data sets were aligned with a nonrigid elastic matching algorithm [15]. In contrast to this elastic model,

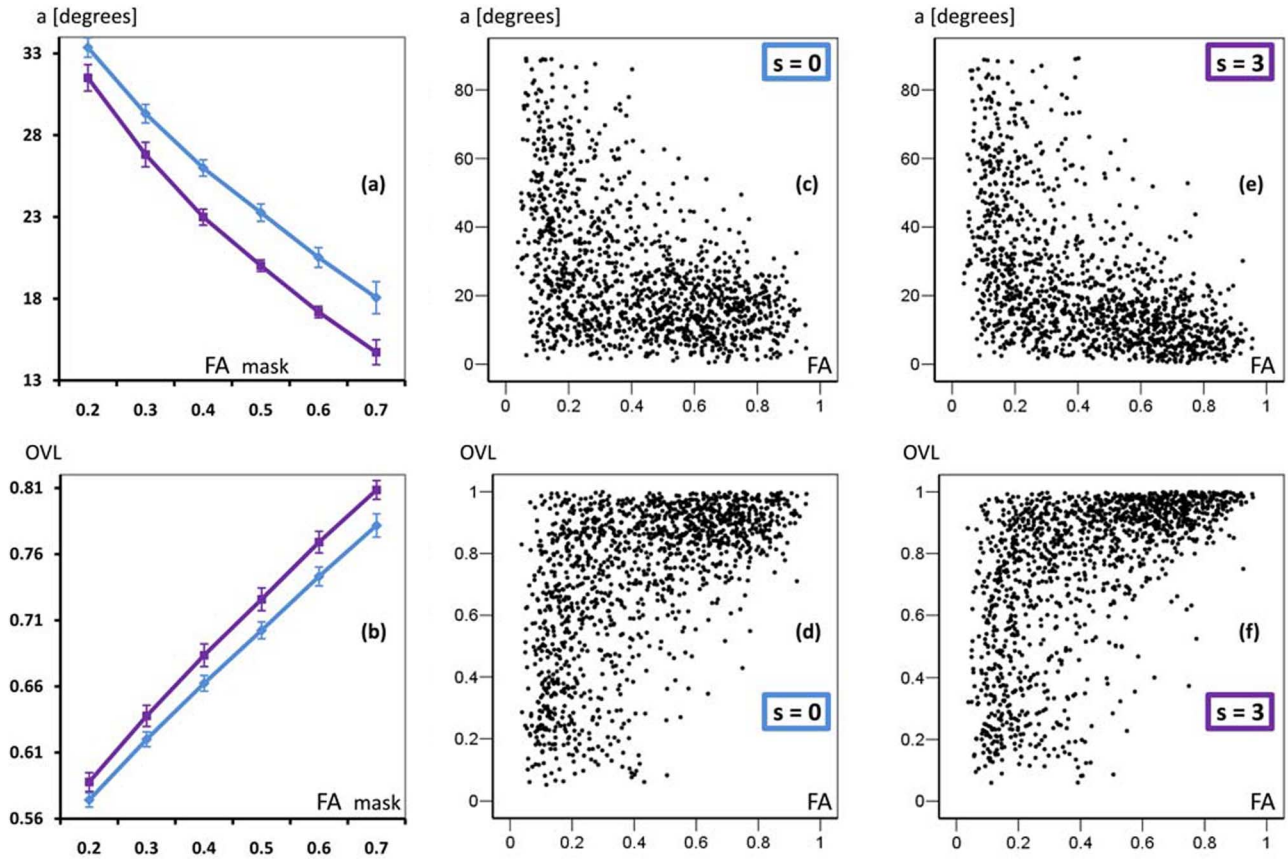

Fig. 11. In (a) and (b), the first eigenvector angle difference a, and OVL are displayed as a function of the threshold that defines the FA mask. To this end, a random subgroup of 10 data sets of different subjects are coregistered based on the FA maps. The FA mask refers to the minimum FA value in a voxel to be included in the quantitative analysis. In blue, the results without smoothing are shown, whereas the purple lines represent the results after a Gaussian smoothing of the deformation field with a kernel width of three voxels. In (c)–(f), scatter plots are displayed. They are obtained from an intersubject coregistration of two DTI data sets. Scatter plots of the FA and a (c) and of the FA and OVL (d) are depicted, containing values of all voxels in a predefined region (a total of 1400 voxels). In (e) and (f), the same scatter plots are displayed, but now after the regularization of the deformation field with a kernel width of three voxels.

the viscous fluid force field relaxes over time. Therefore, the viscous fluid model is a very appropriate regularization method that can correct for the large variations that occur during intersubject coregistration.

Since there are less constraints on a local coregistration level, the Jacobian of the viscous fluid coregistration will be overestimated, resulting in relatively large deformation components. Several results in this paper indicate that small coregistration inaccuracies can result in relatively large tensor orientational differences. We hypothesized that the local coregistration errors will especially contain a deformation component, rather than a rotation factor, resulting in a worse PPD outcome compared to the FS tensor reorientation results. Note that, due to the high correspondence already existing after affine coregistration, the tensor correspondence was still very high when no tensor reorientation was performed after nonrigid alignment. These results appeared to be better than the FS and PPD tensor reorientation results.

In order to tackle this problem and to reduce the effect of local alignment errors on the TR result, a Gaussian regularization procedure was incorporated. As a result, the local alignment inaccuracies were diminished, and the tensor reorientation methods outperformed the approach without a reorientation. Furthermore, since especially the deformation component of the error field has been regularized, the PPD method outperformed the FS approach. In future work, anisotropic filtering methods will be applied to the final deformation field, to investigate the potential improvement of the TR results. Another approach, which will be subject of further research, is to make the TR approach dependent on the local Jacobian.

D. Iterative Tensor Reorientation

The results in Fig. 10 demonstrate that the use of *MI* without an iterative TR is an effective method. Indeed, similar coregistration methodologies, in which an iterative TR was applied, resulted in a worse tensor correspondence. These results agree with the findings of Fig. 7, demonstrating that the tensor correspondence is higher when no TR is performed after coregistration. The tensor differences after FS or PPD reorientation are explained by the effect of small alignment errors on the local Jacobian. In this context, the application of an iterative TR increases the computation time drastically and decreases the tensor correspondence after coregistration.

VI. Conclusion

In this paper, we presented a multicomponent viscous fluid model for the intersubject coregistration of DT images. In the proposed coregistration technique, *MI* was implemented as an

image similarity criterion. Our results demonstrated that the use of orientation information during the coregistration significantly improved the alignment results, compared to the FA based coregistration. A drawback of the local image alignment was that small coregistration inaccuracies can have a relatively large impact on the TR result. In an attempt to minimize these local reorientation errors, we provided a regularization method based on a Gaussian smoothing.

REFERENCES

[1] P. J. Basser, J. Mattiello, and D. LeBihan, "Mr diffusion tensor spectroscopy and imaging," *Biophys. J.*, vol. 66, no. 1, pp. 259–267, Jan. 1994.

[2] C. Beaulieu, "The basis of anisotropic water diffusion in the nervous system—A technical review," *NMR Biomed.*, vol. 15, no. 7–8, pp. 435–455, 2002.

[3] S. Warach, D. Chien, W. Li, M. Ronthal, and R. Edelman, "Fast magnetic resonance diffusion-weighted imaging of acute human stroke," *Neurology*, vol. 42, pp. 1717–1723, 1992.

[4] W. Taylor, E. Hsu, K. Krishnan, and J. MacFall, "Diffusion tensor imaging: Background, potential, and utility in psychiatric research," *Biol. Psychiatry*, vol. 55, pp. 201–207, 2004.

[5] M. Schocke, K. Seppi, R. Esterhammer, C. Kremser, K. Mair, B. Czermak, W. Jaschke, W. Poewe, and G. Wenning, "Trace of diffusion tensor differentiates the parkinson variant of multiple system atrophy and parkinson's disease," *NeuroImage*, vol. 21, pp. 1443–1451, 2004.

[6] N. Barnea-Goraly, H. Kwon, V. Menon, S. Eliez, L. Lotspeich, and A. Reiss, "White matter structure in autism: Preliminary evidence from diffusion tensor imaging," *Biol. Psychiatry*, vol. 55, pp. 323–326, 2004.

[7] J. Burns, D. Job, M. Bastin, H. Whalley, T. Macgillivray, E. Johnstone, and S. Lawrie, "Structural disconnectivity in schizophrenia: A diffusion tensor magnetic resonance imaging study," *Br. J. Psychiatry*, vol. 182, pp. 439–443, May 2003.

[8] S. Rose, F. Chen, J. B. Chalk, F. Zelaya, W. Strugnell, M. Benson, J. Semple, and D. Doddrell, "Loss of connectivity in alzheimer's disease: An evaluation of white matter tract integrity with colour coded MR diffusion tensor imaging," *J. Neurol. Neurosurg. Psychiatry*, vol. 69, pp. 528–530, 2000.

[9] M. Rovaris, A. Gass, R. Bammer, S. Hickman, O. Ciccarelli, D. Miller, and M. Filippi, "Diffusion MRI in multiple sclerosis," *Neurology*, vol. 65, no. 10, pp. 1526–1532, 2005.

[10] M. Kubicki, H. Park, C.-F. Westin, P. Nestor, R. Mulkern, S. Maier, M. Niznikiewicz, E. Connor, J. Levitt, M. Frumin, R. Kikinis, F. Jolesz, R. McCarley, and M. Shentona, "DTI and MTR abnormalities in schizophrenia: Analysis of white matter integrity," *NeuroImage*, vol. 26, no. 4, pp. 1109–1118, 2005.

[11] B. Zitova and J. Flusser, "Image registration methods: A survey," *Image Vision Comput.*, vol. 21, no. 11, pp. 977–1000, Oct. 2003.

[12] W. Crum, T. Hartkens, and D. Hill, "Non-rigid image registration: Theory and practice," *Br. J. Radiol.*, vol. 77, pp. S140–S153, 2004.

[13] U. Bürgel, K. Amunts, L. Hoemke, H. Mohlberg, J. Gilsbach, and K. Zilles, "White matter fiber tracts of the human brain: Three-Dimensional mapping at microscopic resolution, topography and intersubject variability," *NeuroImage*, vol. 29, no. 4, pp. 1092–1105, 2006.

[14] D. Alexander, C. Pierpaoli, P. Basser, and J. Gee, "Spatial transformations of diffusion tensor magnetic resonance images," *IEEE Trans. Med. Imag.*, vol. 20, no. 11, pp. 1131–1139, Nov. 2001.

[15] D. Alexander, J. Gee, and R. Bajcsy, "Strategies for data reorientation during non-rigid warps of diffusion tensor images," *Med. Image Comput. Computer-Assisted Intervention (MICCAI)*, pp. 463–472, 1999.

[16] A. Leemans, J. Sijbers, S. De Backer, E. Vandervliet, and P. Parizel, "Affine coregistration of diffusion tensor magnetic resonance images using mutual information," in *Advanced Concepts for Intelligent Vision Systems*. Berlin, Germany: Springer, 2005, vol. 3708, Lecture Notes Comput. Sci., pp. 523–530.

[17] D. Jones, L. Griffin, D. Alexander, M. Catani, M. Horsfield, R. Howard, and S. Williams, "Spatial normalization and averaging of diffusion tensor MRI data sets," *NeuroImage*, vol. 17, no. 2, pp. 592–617, Oct. 2002.

[18] D. Xu, S. Mori, D. Shen, P. van Zijl, and C. Davatzikos, "Spatial normalization of diffusion tensor fields," *Magn. Reson. Med.*, vol. 50, no. 1, pp. 175–182, Jul. 2003.

[19] D. Alexander, J. Gee, and R. Bajcsy, "Elastic matching of diffusion tensor mris," in *Proc. 1999 IEEE Comput. Soc. Conf. Comput. Vision Pattern Recognition*, Fort Collins, CO, 1999, pp. 244–249.

[20] J. Ruiz-Alzola, C. Westin, S. Warfield, A. Nabavi, and R. Kikinis, "Nonrigid registration of 3D scalar, vector and tensor medical data," *Med. Image Comput. Computer-Assisted Intervention*, vol. 1935, pp. 541–550, 2000.

[21] J. Ruiz-Alzola, C.-F. Westin, S. Warfield, C. Alberola, S. Maier, and R. Kikinis, "Nonrigid registration of 3D tensor medical data," *Med. Image Anal.*, vol. 6, pp. 143–161, 2002.

[22] A. Guimond, C. Guttmann, S. Warfield, and C.-F. Westin, "Deformable registration of DT-MRI data based on transformation invariant tensor characteristics," in *Proc. IEEE Int. Symp. Biomed. Imag. (ISBI'02)*, Washington, DC, , 2002, pp. 761–764.

[23] H.-J. Park, M. Kubicki, M. Shenton, A. Guimond, R. McCarley, S. Maier, R. Kikinis, F. Jolesz, and C.-F. Westin, "Spatial normalization of diffusion tensor MRI using multiple channels," *NeuroImage*, vol. 20, no. 4, pp. 1995–2009, 2003.

[24] J.-P. Thirion, "Image matching as a diffusion process: An analogy with maxwell's demons," *Med. Image Anal.*, vol. 2, no. 3, pp. 243–260, Sep. 1998.

[25] H. Zhang, P. Yushkevich, D. Alexander, and J. Gee, "Deformable registration of diffusion tensor MR images with explicit orientation optimization," *Med. Image Anal.*, vol. 10, no. 5, pp. 764–785, 2006.

[26] E. D'Agostino, F. Maes, D. Vandermeulen, and P. Suetens, "A viscous fluid model for multimodal non-rigid image registration using mutual information," *Med. Image Anal.*, vol. 7, no. 4, pp. 565–575, Dec. 2003.

[27] Y. Wang and L. Staib, "Physical model-based non-rigid registration incorporating statistical shape information," *Med. Image Anal.*, vol. 4, no. 1, pp. 7–20, Mar. 2000.

[28] A. Collingnon, F. Maes, D. Delaere, D. Vandermeulen, P. Suetens, and G. Marchal, "Automated multimodality medical image registration using information theory," in *Proc. Int. Conf. Inf. Process. Med. Imag.: Computational Imag. Vision*, 1995, pp. 263–274.

[29] W. Wells, P. Viola, H. Atsumi, S. Nakajima, and R. Kikinis, "Multimodal volume registration by maximization of mutual information," *Med. Image Anal.*, vol. 1, no. 1, pp. 35–51, Mar. 1996.

[30] F. Maes, A. Collignon, D. Vandermeulen, G. Marchal, and P. Suetens, "Multimodality image registration by maximization of mutual information," *IEEE Trans. Med. Imag.*, vol. 16, no. 2, pp. 187–198, Apr. 1997.

[31] G. Hermosillo, C. C. d'Hotel, and O. Faugeras, "Variational methods for multimodal image matching," *Int. J. Comput. Vis.*, vol. 50, no. 3, pp. 329–343, 2002.

[32] G. E. Christensen, R. D. Rabbitt, and M. I. Miller, "Deformable templates using large deformation kinematics," *IEEE Trans. Image Process.*, vol. 5, no. 10, pp. 1435–1447, Oct. 1996.

[33] M. Bro-Nielsen and C. Gramkow, "Fast fluid registration of medical images," in *Visualization in Biomedical Computing (VBC'96)*, R. Kikinis and K. Hoehne, Eds. Berlin: Springer-Verlag, 1996, vol. 1131, Lecture Notes Computer Science, pp. 267–276.

[34] V. Noblet, C. Heinrich, F. Heitz, and J. Armspach, "Retrospective evaluation of a topology preserving non-rigid registration method," *Med. Image Anal.*, vol. 10, no. 3, pp. 366–384, 2006.

[35] A. Anderson, *Theor. Anal. Effects Noise Diffusion Tensor Imaging*, vol. 46, no. 6, pp. 1174–1188, Dec. 2001.

[36] T. Han, "Multiple mutual informations and multiple interactions in frequency data," *Inf. Control*, vol. 46, no. 1, pp. 26–45, 1980.

[37] G. Rohde, S. Pajevic, C. Pierpaoli, and P. Basser, "A comprehensive approach for multi-channel image registration," in *Second International Workshop on Biomedical Image Restoration (WBIR03)*. New York: Springer, 2003, vol. 2717, pp. 214–223.

[38] D. Jones, "The effect of gradient sampling schemes on measures derived from diffusion tensor MRI: A monte carlo study," *Magn. Reson. Med.*, vol. 51, pp. 807–815, 2004.

[39] A. Leemans, J. Sijbers, and P. Parizel, "A graphical toolbox for exploratory diffusion tensor imaging and fiber tractography," presented at the 14th Annu. Meeting-Section Magn. Reson. Technologists, Miami, FL, 2005.

[40] P. J. Basser and S. Pajevic, "Statistical artifacts in diffusion tensor MRI (DT-MRI) caused by background noise," *Magn. Reson. Med.*, vol. 44, pp. 41–50, Jul. 2000.

[41] A. Leemans, J. Sijbers, M. Verhoye, A. Van der Linden, and D. Van Dyck, "Mathematical framework for simulating diffusion tensor MR neural fiber bundles," *Magn. Reson. Med.*, vol. 53, pp. 944–953, 2005.

[42] L. Malvern, *Introduction to the Mechanics of a Continuous Medium*. Englewood Cliffs, NJ: Prentice-Hall, 1969.

[43] V. Arsigny, P. Fillard, X. Pennec, and N. Ayache, "Log-Euclidean metrics for fast and simple calculus on diffusion tensors," *Magn. Reson. Med.*, vol. 56, no. 2, pp. 411–421, 2006.